System-Level Large-Signal Stability Analysis of Droop-Controlled DC Microgrids

Xie, Wenqiang; Han, Minxiao; Cao, Wenyuan; Guerrero, Josep M.; Vasquez, Juan C.

System-Level Large-Signal Stability Analysis of Droop-Controlled DC Microgrids

Wenqiang Xie, *Student Member, IEEE*, Minxiao Han, *Senior member*, *IEEE*, Wenyuan Cao, *Student Member, IEEE*, Josep M. Guerrero, *Fellow, IEEE*, and Juan C. Vasquez, *Senior member*, *IEEE*

Abstract—In the literature, many studies on stability analysis of dc microgrid have been conducted. However, most of them mainly focus on small-signal stability. On the other hand, few works analyze large-signal stability, but the major part of these works is based on a single unit or a simple cascaded system as a case study. Different from those, this paper aims to address the large-signal stability analysis of a dc microgrid from a system-level perspective. First, the equivalent model of a droop-controlled dc microgrid is developed. Subsequently, the Lyapunov-based large-signal stability analysis and the stability criterion are derived, and mixed potential theory is used to make comparisons to verify the effectiveness of derived criterion. The equilibrium point stability for different operation stages was obtained by means of theoretical calculation. Further, the instabilities principle as well as their physical interpretation are revealed. In this work, the bus voltage is used as the only index to assess the microgrid power balance. Hence, the power load limit can be obtained by taking into consideration the stability and voltage deviation constraints. Finally, simulation and experimental results from a 4-converter dc microgrid system verify the feasibility of the proposed theoretical analysis.

Index Terms—dc microgrids, large-signal stability, Lyapunov function, droop control.

I. INTRODUCTION

AS an effective way to seamlessly integrate and utilize distributed energy resources, dc microgrids have been extensively studied over the past 10 years [1], [2]. These have been used in so many fields, including the power grid, industry, greenhouse, traffic, etc. Although dc microgrids have many benefits, many drawbacks still exist [3]-[5]. Stability is a vital issue that cannot be ignored as its weak inertia and damping [6]-[8]. Many studies about stability have been conducted through small-signal analysis (SSA) and large-signal analysis (LSA) [9]-[11].

SSA is based on linearizing the nonlinear system around an equilibrium point, and the linearized system is then studied by linear analysis tools such as eigenvalue, Nyquist, and Routh stability criterion. It has been widely applied in a single unit,

including motors, inverters, and rectifiers, to improve parameter design in controllers [12], [13]. However, the main drawback of SSA is that its validity and effectiveness are limited to a tiny domain around an equilibrium point, without accurate indication of how large the tiny domain is. Moreover, the parameters designed by SSA are only accurate at a certain equilibrium point, but the equilibrium point is frequently changed as pulse power load operation and load switching.

Large power disturbances in dc microgrids are inevitable such as loss of distributed sources, large load variations, and circuit faults [14], hence LSA is much necessary. LSA adopts nonlinear mathematical methods without linearization, whose complexity is determined by the order of the system, and the domain of which is much larger than that of SSA. Many studies have been done about LSA in recent years, but most of them focus on one unit or a cascaded system [15]-[18], thus not being appropriated for a system level. In this sense, [16] describes a dc microgrid as a cascaded system by a single source in connection with constant power load (CPL), and then optimizes parameter design based on double close loop control, not suitable for the multi-source parallel system. For instance, in [17], [18] a control parameter determination method for grid-forming converters (GC) is proposed to stabilize the system under large-signal disturbances. The premise of this method is that the capacity of a single energy storage unit should be large enough since this approach can be only used for one voltage source [19].

Further, in [16] LSA is used to estimate the domain of asymptotic stability of dc microgrids, but it mainly concentrates on the parameter design of the grid-connected inverter. On the other hand, usually, the capacity of the ac grid is large enough, hence it is commonly stable in grid-connected mode. Hence more efforts should be put into the studies on islanded dc microgrids modeling. This paper focuses on island dc microgrids stability modeling and analysis. With the scale-up of dc microgrids, more than one GC requires the parallel operation to provide enough capacity and redundancy. In this sense, droop controller is widely employed in many studies [19], [20], which allows circulating current reduction among

converters and can easily realize power-sharing and voltage regulation [21]-[23]. Thus, the single voltage-source model is no more appropriate for those multiple voltage-source converter systems. Most studies using single voltage-source models are engaged in optimizing PI controller parameters design [16]-[18]. However, a dc microgrid is a more complex system as shown in Fig.1, in which lots of converters coexist. Each of them has its own proportional and integral parameters, which are usually set by the designer and unknown to the users. Thus, it is not practical to figure out one parameters-set as the equivalent value, being then multi-GC parallel system taken into consideration in this paper.
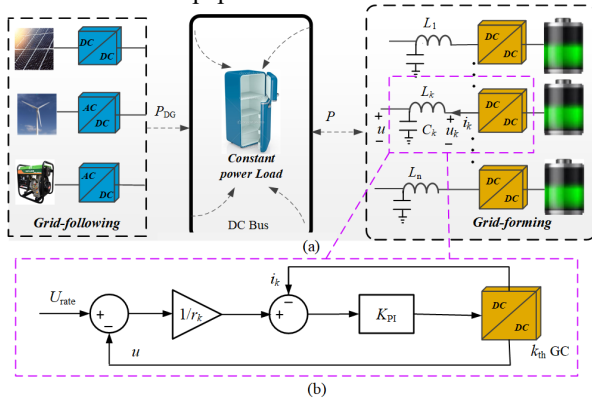

Fig. 1. Typical structure of dc microgrid and droop controller. (a) Typical structure. (b) droop controller of k_{th} GC.

Many studies have illustrated that CPLs exhibit negative impedance characteristics, thus threatening the stable operations of dc microgrids. CPLs are commonly referred to those power electronic loads and motors with tight regulation, and so on. They present negative impedances to the dc bus within their control bandwidths and unfavorably interact with source converters [25], [26]. Considering CPLs have more negative influences than resistive load, the extremely worst situation that all loads are CPLs is studied in this paper, making dc microgrids a nonlinear system.

Several methods can be used in LSA of nonlinear systems, including the Lyapunov direct method, Takagi-Sugeno fuzzy model method (TS), block diagonalized quadratic Lyapunov function (BDQLF), reverse trajectory tracking method, and mixed potential theory (MPT), but each of them has shortcomings. The Lyapunov direct method is the most widely used approach in estimating region of attraction [11], [20], [24], [27], although the derived stability criterion is commonly conservative. However, this drawback can be easily overcome in this work. The TS [28] and BDQLF [29] are derived from the Lyapunov direct method, which share the same problem of the conservative criterion. Additionally, the computational complexity of TS increases exponentially with the number of nonlinearities, making TS ill-suited for higher-order systems. The reverse trajectory tracking method [30] is a graphical approach and cannot be derived in an analytic form. MPT is another commonly utilized method in recent years [15], [16], [31], but its criterion is not as detail as that derived by the Lyapunov direct method in this work, and it is hard to rigidly prove the necessity of the second condition in studies. Therefore, the Lyapunov direct method is adopted in this paper,

and conservatism-free is achieved mathematically. Besides, to illustrate the advantages of the Lyapunov direct method, MPT is employed in Section III to make comparisons.

This paper is organized as follows. Section II develops the system model according to the operation strategy with droop control. Section III establishes the Lyapunov function to analyze large-signal stability, then the sufficiency and necessity criterion is derived. To tell the advantages of the Lyapunov direct method, MPT is employed to make comparisons. In Section IV, the stability of equilibrium points in different stages is discussed, and its physical interpretation is clearly explained. Furthermore, the limit of power load is proposed in Section V within the constraints of stability and voltage deviation. Simulation and experimental results are provided in Section VI to enhance the correctness of the theoretical analysis. Conclusions are drawn in Section VII.

II. LARGE-SIGNAL MODEL OF DC MICROGRIDS

A. Grid-Forming Converters Modeling

Dc microgrids consist of distributed power sources, energy storage systems, and power loads, as shown in Fig. 1. With the scaling-up of dc microgrids, energy storage system requires more parallel-connected GCs to maintain power balance [32], [33]. Hence, droop control is widely employed. The voltage droop control can be implemented in a virtual-resistance way as following

$$u = U_{rate} - ri, \tag{1}$$

where U_{rate} is the rated voltage, u is the bus voltage, i is the load current, and r is virtual resistance. According to (1), the external characteristic of droop control can be thought as the series connection of dc source and virtual resistance.
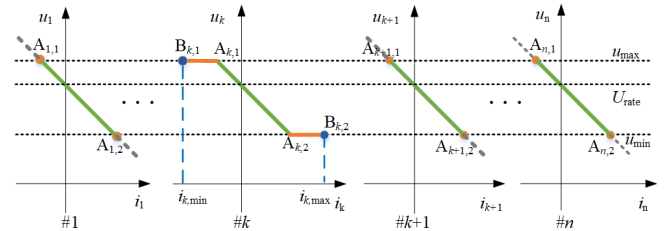
Fig. 2. The schematic diagram of control strategy of multi-GC parallel operation

Assuming n GCs parallel operation in a dc microgrid and each adopting drool control strategy, the control curve can be shown in Fig. 2, where $n \in N= \{1, 2, ..., n\}$. Considering the requirement of insulation, devices operation, etc., the voltage deviation must be limited within a reasonable range. Besides, in order to avoid huge circulation caused by control deviations when parallel operation, only one GC (the master GC) can employ constant voltage strategy. Only if this GC fails to normal operation, one of the other GCs can adopt the constant voltage strategy in accordance with certain priorities. Therefore, the operation process can be divided into two stages as shown in Fig. 2. In the first stage, voltage deviation doesn't reach any bound, so that all GCs adopt droop control. In the second stage, voltage deviation reaches upper or lower bound, thus one GC adopts constant voltage strategy and the others adopt constant

current strategy. For convenient expression, here define two types of operating points A and B, where A is determined by voltage/current limitations and B by the converter capacity. Taking k_{th} GC as an example, $[A_{k1}, A_{k,2}]$ is for droop control strategy, $[B_{k1}, A_{k,1}]$ and $[A_{k2}, B_{k,2}]$ are for constant voltage strategy.

1). Modeling for the first stage. In the first stage, all GCs adopt droop control strategy. As shown in Fig. 1, the transient control model of k_{th} GC can be expressed as

$$\frac{di_k}{dt} = \frac{1}{L_k}(U_{rate} - u - r_k i_k),\qquad(2)$$

where i_k is the output current of k_{th} GC, L_k is the output side inductance in series with k_{th} GC, and r_k is the virtual resistance of k_{th} GC.

Assuming i_{eq} as the output current of the entire energy storage system, it can be expressed as

$$i_{eq} = \sum_{k=1}^{n} i_k = (U_{rate} - u)\sum_{k=1}^{n}\frac{1}{r_k}.\qquad(3)$$

Hence, the equivalent virtual resistance can be expressed as

$$r_{eq} = 1 \Big/ \sum_{k=1}^{n}\frac{1}{r_k}.\qquad(4)$$

Considering the condition in design [23]

$$\frac{r_1}{L_1} \approx \frac{r_2}{L_2} \approx \cdots \approx \frac{r_n}{L_n},\qquad(5)$$

then, we can obtain the equivalent current dynamics by combining (3)-(5), as

$$\frac{di_{eq}}{dt} = (U_{rate} - u)\sum_{k=1}^{n}\frac{1}{L_k} - i_{eq}\sum_{k=1}^{n}\frac{1}{L_k}\Big/\sum_{k=1}^{n}\frac{1}{r_k}.\qquad(6)$$

Thus, the equivalent inductance L_{eq} can be approximately given by

$$L_{eq} = 1 \Big/ \sum_{k=1}^{n}\frac{1}{L_k}.\qquad(7)$$

Then (6) can be reformulated as

$$\frac{di_{eq}}{dt} = \frac{1}{L_{eq}}(U_{rate} - u - r_{eq}i_{eq}).\qquad(8)$$

Therefore, a multi-GC parallel operation storage system adopting drool control can be also equivalent to the series connection of dc source, virtual resistance, and filter inductance, as shown in Fig. 3(a).

2). Modeling for the second stage. In the second stage, the k_{th} GC operates in constant voltage mode, where the output current is determined by power load. Besides, the other GCs will work in constant current mode because the bus voltage is constant. Hence, the equivalent circuit can be modeled as the series connection of dc source and filter inductance, and then parallel connected to a controlled current source, as shown in Fig. 3(b). The total output current and power of the other GCs can be separately represented by i_{oth} and P_{oth} as

$$P_{oth} = i_{oth} \cdot U_{lim} = U_{lim} \cdot \sum_{m \neq k} i_m,\qquad(9)$$

where U_{lim} is the limited value of voltage deviation. The other GCs operate as negative power load relative to the k_{th} GC.

B. Modeling for Equivalent Power Load

In order to maximize the utilization of renewable energy, distributed sources mostly operate in maximum power point tracking (MPPT) mode, which show like the reverse power loads relative to the energy storage system. It is positive when power flows to energy storage system from distributed energy and symbolled by P_{DG}.

As aforesaid, the dc load in the dc microgrids exhibits constant power characteristics due to its power electronic converters with a tight feedback controller. From the perspective of the system, the dc load can be equivalent to the power load that varies with the usage behavior of electricity and expressed by P_{load}.

Therefore, the distributed power source and the dc load can be equivalent to a bidirectional power load P_L, expressed as

$$P_L = P_{load} - P_{DG}.\qquad(10)$$
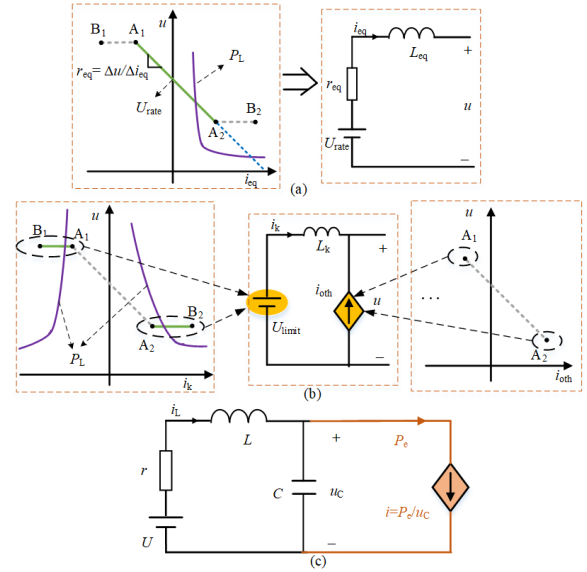
Fig. 3. The equivalent model of DC microgrid. (a) Equivalent circuit of the first stage. (b) Equivalent circuit of the second stage. (c) Normalized equivalent model of two stages.

C. Equivalent Model of DC Microgrids

Based on the above analysis, considering the capacitance parallel to the energy storage system, distributed energy, grid-connected unit and dc bus, the normalized equivalent model of two stages of dc microgrids can be expressed as Fig. 3(c), where U the equivalent dc voltage source, r the equivalent virtual resistance, L the equivalent inductance, P_e the equivalent constant power load, and C the equivalent capacitance connected in parallel to the dc bus. Besides, u_C is capacitance voltage, i.e., the bus voltage, i_L is inductance current, $i=P/u_C$ is equivalent load current, and $i=i_L$ in the steady-state.

It is easy to conclude that the means of variables in the first stage and second stage separately are

$$\text{first stage}\begin{cases}U = U_{rate}\\ r = r_{eq}\\ L = L_{eq}\\ P_e = P_L\end{cases},\ \text{second stage}\begin{cases}U = U_{lim}\\ r \to 0\\ L = L_k\\ P_e = P_L - P_{oth}\end{cases}.\qquad(11)$$

III. LARGE-SIGNAL STABILITY CRITERION

The Lyapunov function is established in this section to analyze large-signal stability of dc microgrids, and MPT is employed to make comparisons with it. The results show that the Lyapunov direct method is more suitable for this work.

A. LSA Based on the Lyapunov Direct Method

Assuming $x_e = [i_{Le},\ u_{Ce}]^T$ as the equilibrium point of the system, and $\Delta x = [\Delta i_L,\ \Delta u_C]^T$ as variation, the mathematical model of dc microgrids can be derived as

$$\begin{cases} \dfrac{d(\Delta i_L)}{dt} = \dfrac{1}{L}(-r\Delta i_L - \Delta u_C) \\ \dfrac{d(\Delta u_C)}{dt} = \dfrac{1}{C}\left(\Delta i_L + \dfrac{P_e}{u_{Ce}^2}\Delta u_C\right) \end{cases}. \tag{12}$$

Its matrix form is

$$\Delta \dot{x} = J\Delta x, \tag{13}$$

where

$$J = \begin{bmatrix} -r/L & -1/L \\ 1/C & P_e/Cu_C^2 \end{bmatrix}_{x_e}. \tag{14}$$

According to the Lyapunov direct method, for a given nonlinear system, if a Lyapunov function $V(x)$ is found to be a positive definite matrix and meanwhile its derivative is a negative definite matrix, then the system is of small-signal stability at the equilibrium point. In addition, when $\|x\| \to \infty$, $V(x) \to \infty$ is further satisfied, the system is believed large-signal stable. For the system built as (12)-(14), that $x = [i_L,\ u_C]^T$ is selected as state variables, and then the equation of state can be expressed as

$$\dot{x} = \Phi(x) \tag{15}$$

and

$$\dot{\Phi}(x) = \frac{\partial \Phi(x)}{\partial x}\dot{x} = J\Phi(x), \tag{16}$$

where

$$\Phi(x) = \begin{bmatrix} \phi_1 \\ \phi_2 \end{bmatrix} = \begin{bmatrix} (U - ri_L - u_C)/L \\ (i_L - P_e/u_C)/C \end{bmatrix}. \tag{17}$$

The Lyapunov function can be constructed as

$$V(x) = \dot{x}^T H\dot{x} = \Phi(x)^T H\Phi(x), \tag{18}$$

where H is positive definite, hence $V(x)$ is also positive definite. The full derivative of $V(x)$ for t is calculated as

$$\dot{V}(x) = -\Phi(x)^T Q(x)\Phi(x), \tag{19}$$

and

$$Q(x) = -[J^T H + HJ]. \tag{20}$$

In order to ensure the progressive stability of the system under small disturbance, the negative definiteness of $\dot{V}(x)$ must be guaranteed. Therefore, set $Q(x)=I$, then H can be derived as

$$H = \begin{bmatrix} h_a & h_b \\ h_b & h_c \end{bmatrix} = \frac{I + det(J)(JJ^T)^{-1}}{-2Tr(J)}, \tag{21}$$

where $det(J)$ is the determinant of J, $Tr(J)$ is the trace of J, and I is the unit matrix. The symbolic expression of H can be seen in the Appendix (1)-(3).

To ensure positive definiteness of H, it should be satisfied

$$\begin{cases} \Delta_1 = h_a > 0 \\ \Delta_2 = h_a h_c - h_b^2 > 0 \end{cases}, \tag{22}$$

which means

$$\begin{cases} rP_e - u_C^2 < 0 \\ LP_e - Cu_C^2 r < 0 \end{cases}. \tag{23}$$

That is, under the condition of (23), the system is of small-signal stability.

To further verify the stability of system under large disturbance, H is rewritten as

$$H = \begin{bmatrix} h_{a0} + h_{a1} & h_b \\ h_b & h_{c0} + h_{c1} \end{bmatrix}. \tag{24}$$

It can be seen from (22) and (24) that there is $h_{a0}h_{c0}=h_b^2$ and $min\{h_{a0}, h_{a1}, h_{c0}, h_{c1}\} \geq 0$ existing simultaneously. Therefore, $V(x)$ can be expressed as

$$\begin{aligned} V(x) &= h_a\phi_1^2 + 2h_b\phi_1\phi_2 + h_c\phi_2^2 \\ &= (\sqrt{h_{a0}}\phi_1 + \sqrt{h_{c0}}\phi_2)^2 + h_{a1}\phi_1^2 + h_{c1}\phi_2^2 \end{aligned}. \tag{25}$$

Obviously, when $\|x\| \to \infty$, $V(x) \to \infty$ will be satisfied. This means, under the condition of (23), the system is of large-signal stability.

B. Supplementary Explanation of Sufficiency and Necessity

The shortcoming of the Lyapunov direct method is conservatism. In other words, it can only explain the sufficiency of (23) and cannot explain its necessity. Here, we give its necessity as follows.

For the second-order system given by (14), the necessary and sufficient criterion for small-signal stability is

$$\begin{cases} \text{Tr}(J) < 0 \\ |J| > 0 \end{cases}, \tag{26}$$

which can be simplified as

$$\begin{cases} rP < u_C^2 \\ LP < Cu_C^2 r \end{cases}. \tag{27}$$

It is obvious that (27) is the transformation of (23), which means (23) is also the necessary and sufficient criterion for small-signal stability. In addition, if a system is of large-signal stability, it must first be of small-signal stability. Hence formula (23) is the both necessary and sufficient criterion for large-signal stability. The second sub-formula of (23) can be also derived by MPT, but the first one cannot. The detailed comparisons are shown in the following content.

C. Comparisons with MPT

From the law of *MPT* [30] (detailed in Appendix (4)-(9)), the mixed potential function in this work can be constructed as

$$P(i_L, u_C) = -\frac{1}{2}ri_L^2 + \int_0^{u_C}\frac{P_e}{u_C}du_C + i_L(U_{rate} - u_C), \tag{28}$$

where

$$A(i_L) = \frac{1}{2}ri_L^2,\ B(u_C) = \int_0^{u_C}\frac{P_e}{u_C}du_C,\ (i, \gamma v - \alpha) = i_L(U_{rate} - u_C),$$

and $A_{ii}(i) = \dfrac{\partial^2 A(i_L)}{\partial i_L^2} = r,\ B_{vv}(u_C) = \dfrac{\partial^2 B(u_C)}{\partial u_C^2} = \dfrac{-P_e}{u_C^2}.$

Defining μ_1 the minimum eigenvalue of matrix $L^{-1/2}A_{ii}(i_L)\,L^{1/2}$, μ_2 the minimum eigenvalue of matrix $C^{-1/2}B_{vv}(u_C)\,C^{1/2}$, μ_1 and μ_2 can be calculated as

$$\mu_1 = \frac{r}{L}, \ \mu_2 = \frac{-P_e}{Cu_C^2}. \tag{29}$$

To make system stable, it should firstly satisfy

$$\mu_1 + \mu_2 = \frac{r}{L} - \frac{P_e}{Cu_C^2} > 0 \Rightarrow LP_e - Cu_C^2 r < 0, \tag{30}$$

which is the same as the second sub-formula of (23). Secondly, it should simultaneously satisfy when $|i_L|+|u_C|\to\infty$, $P^*(i_L, u_C)\to\infty$. In this work, $P^*(i_L, u_C)$ is expressed as

$$P^*(i_L, u_c) = \frac{1}{2}\left(\frac{r}{L} + \frac{P_e}{Cu_C^2}\right)\left(-\frac{1}{2}ri_L^2 + \int_0^{u_c}\frac{P_e}{u_C}du_C + i_L\left(U_{rate} - u_C\right)\right)$$
$$+ \frac{1}{2L}\left(-ri_L + U - u_C\right)^2 + \frac{1}{2C}\left(\frac{P_e}{u_C} - i_L\right)^2.$$

When $|i_L|+|u_C|\to\infty$, $P^*(i_L, u_C)$ can be simplified as

$$P^*(i_L, u_C) = \underbrace{\frac{i_L^2}{2}\left(\frac{1}{C} + \frac{r^2}{2L}\right)}_{\infty} + \underbrace{\frac{-r}{4L}i_L u_C}_{-\infty}. \tag{31}$$

It not easy to rigidly judge $P^*(i_L, u_C) \to \infty$.

Hence, compared with the Lyapunov direct method, MPT is more difficult when using in this work, and the criterion is not as comprehensive as (23) because it cannot derive the first sub-formula of (23), but the first one is necessary illustrated as (47). Therefore, (23) is taken as the stability criterion in this work. The comparisons are listed in Table I.

TABLE I
COMPARISONS BETWEEN TWO METHODS

Compared items	MPT	Lyapunov direct method
Criterion	$LP_e - Cu_C^2 r < 0$	$\begin{cases} rP_e - u_C^2 < 0 \\ LP_e - Cu_C^2 r < 0 \end{cases},$ more comprehensive
Derivation process	Not rigid	Perfectly rigid

IV. STABILITY ANALYSIS AND PHYSICAL INTERPRETATION

The studied system is of large-signal stability under the condition of (23), but more than one equilibrium point exists in mathematical solutions, as shown in Fig. 4. Due to the droop control characteristics, the output current of the energy storage system is a linear function of the bus voltage, whose slope is r and the intercept is U_{rate}, as shown by the straight line. The equivalent CPLs can be positive or negative, and the load current is inversely proportional to the bus voltage. If the equivalent CPLs are positive, the power curve and the droop control curve will intersect in the first quadrant. Otherwise, if the equivalent power load is negative, the two curves will intersect in the second and fourth quadrants. However, since the bus voltage cannot be negative, the intersection of the fourth quadrant will be ignored. Thus, only the stability of the upper half-plane equilibrium points (i.e., a, b, c, d, e shown in Fig. 4) will be discussed.

The equilibrium points of the system can be derived as

$$\begin{cases} \boldsymbol{x}_{e1} = \begin{bmatrix} i_{Le1} & u_{Ce1} \end{bmatrix} = \begin{bmatrix} P_e/u_{Ce1} & (U+w)/2 \end{bmatrix} \\ \boldsymbol{x}_{e2} = \begin{bmatrix} i_{Le2} & u_{Ce2} \end{bmatrix} = \begin{bmatrix} P_e/u_{Ce2} & (U-w)/2 \end{bmatrix} \end{cases}, \tag{32}$$

where

$$\begin{cases} w = \sqrt{U^2 - 4rP_e} \\ P_e < U^2/(4r) = P_{max} \end{cases}. \tag{33}$$

It can be easily known from the derivation process that a, b, c, and $d \in x_{e1}$, whereas $e \in x_{e2}$.

For the convenience of analysis, formula (24) is rewritten as

$$P_e < r^2 C/L \cdot (u_C^2/r) \tag{34}$$

and

$$P_e < u_C^2/r. \tag{35}$$

That is, if the system is to maintain the large-signal stability, it must satisfy both (30) and (31) simultaneously.
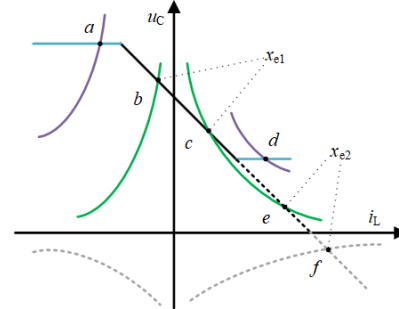

Fig. 4. The distribution of DC microgrid equilibrium points.

From (34) and (35), it is obvious when $P_e < 0$, the system is always in a stable state, which means points a and b are always in the stable state. On the other hand, when $P_e > 0$, the stability of the system cannot be directly seen. From Section II, in the second stage, r is infinitely close to 0. However, in a practical microgrid system, considering the resistance of lines and other devices, r will not completely be zero. Besides, c and $d \in x_{e1}$, thus the stability constraint of point d should be consistent with c. Thus, only stability of point c and e will be analyzed below.

A. Stability Analysis of Point c

From (30) and (31), it can be seen when $L < r^2 C$, x_{e1} only needs to satisfy (35). Substituting x_{e1} into (35) and making simplification, it can be derived as

$$w^2 + U_{rate} w > 0. \tag{36}$$

Obviously, under the condition of (29), (36) is always satisfied. That is, when $L < r^2 C$, for $\forall P_e < P_{max}$, the system is always stable.

On the other hand, when $L > r^2 C$, x_{e1} only needs to satisfy (34). Substituting x_{e1} into (30), it can be simplified as

$$(2L + 2r^2 C)/(rC) \cdot P_e - U_{rate}^2 < U_{rate} w. \tag{37}$$

If the equivalent CPLs satisfy

$$P_e < \frac{2r^2 C}{L + r^2 C} \cdot P_{max}, \tag{38}$$

then (37) will always be satisfied. Otherwise, P_e needs to satisfy

$$\frac{2r^2 C}{L + r^2 C} \cdot P_{max} < P_e < \frac{2r^2 C}{L + r^2 C} - \frac{2L}{L + r^2 C} \cdot P_{max}. \tag{39}$$

Particularly, it is easy to prove that

$$2L/(L + r^2 C) > 1. \tag{40}$$

Hence, the inequality relationship of (39) is correctly established.

In summary, when $L>r^2C$, the system is of large-signal stability under the condition of

$$P_e < 4r^2CL\big/\left(L+r^2C\right)^2 \cdot P_{\max} = P'_{\max} . \tag{41}$$

B. Stability Analysis of Point e

When $L<r^2C$, x_{e2} only needs to satisfy (35). Substitute x_{e2} into (35) and it can be simplified as

$$w\left(w-U_{\text{rate}}\right) > 0 . \tag{42}$$

Obviously, for $\forall P_e > 0$, formula (42) would never be satisfied.

On the other hand, when $L>r^2C$, x_{e2} can automatically satisfy (34). However, for $\forall P_e > 0$, formula (42) would never be satisfied. Hence, the system is unstable at point e.

C. Physical Interpretation of Equilibrium Points

To summarize above analysis, equilibrium points of dc microgrids can be divided into three types, shown as Fig. 5, where point a and b are classified into the first type, point c and d are classified into the second type, and point e is classified into the third type.

1). The first type. The equilibrium point in Fig. 5(a) shows the characteristics of $P_e < 0$. Assuming the system is in steady-state at this point, if any disturbance occurs at the same time, the bus voltage will have a disturbance increment. If the increment is negative, the current from negative power load to the dc bus will increase according to the power curve but is simultaneously larger than the current needed by droop control, that is $i-i_L<0$. At this time, the extra current will flow into the parallel capacitor causing the bus voltage to rise. Otherwise, if the increment is positive, the physical process will be similar. Hence, the system is of large-signal stability when operating at points of this type. From Fig. 5(a), mathematical description of the first type can be derived as

$$\frac{di_L}{du_C} < 0 < \frac{di}{du_C} , i_{Le} < 0 . \tag{43}$$

2). The second type. The equilibrium point in Fig. 5(b) shows the characteristics of $P_e > 0$. Assuming the system is in steady-state at this point, and if any disturbance occurs at this time, the bus voltage will have a disturbance increment. If the increment is negative, the needed load current will increase but is still smaller than the output current by droop control, that is $i-i_L<0$, the extra current will flow into parallel capacitor bringing about the rise of the bus voltage. Otherwise, if the increment is positive, the physical process will be similar. Hence, the system is of large-signal stability when operating at points of this type. From Fig. 5(b), mathematical description of the second type can be derived as

$$\frac{di_L}{du_C} < \frac{di}{du_C} < 0, i_{Le} > 0 . \tag{44}$$

3). The third type. The equilibrium point in Fig. 5(c) is not of large-signal stability, analyzed as follows. Assuming the system is in steady-state at this point, and if any disturbance occurs at this time, the bus voltage will have a disturbance increment. If the increment is negative, the needed load current will increase

and is unfortunately larger than the output current by droop control, that is $i-i_L>0$. The capacitor will discharge to make up the discrepancy leading to a further decline of the bus voltage. Otherwise, if the increment is positive, the physical process will be similar. Hence, the system is not of large-signal stability when operating at points of this type. The mathematical description of the second type can be derived as

$$\frac{di}{du_C} < \frac{di_L}{du_C} < 0, i_{Le} > 0 . \tag{45}$$

4). Summary. Through the analysis of the above physical process, it can be found that the essence of the first and second type is that the polarity of bus voltage change is opposite to the polarity of the current change flowing into the capacitor. In other words, the control process can make up the bus voltage disturbance increment, as shown in Fig. 5(d). Thus, the mathematical model can be expressed as

$$\Delta u_C \cdot \left(\Delta i_L - \Delta i\right) < 0 , \tag{46}$$

which can be rewritten as

$$\frac{di_L}{du_C} < \frac{di}{du_C} \Rightarrow rP_e - u_C^2 < 0 . \tag{47}$$

It is consistent with (43) and (44).

The above analysis figures out the necessary criterion of stability from the aspects of control process and physical meaning, but is not of sufficiency. The effect of the physical parameters such as L and C of the system itself on stability should still be considered, so that the second sub-formula in (23) should be also satisfied.
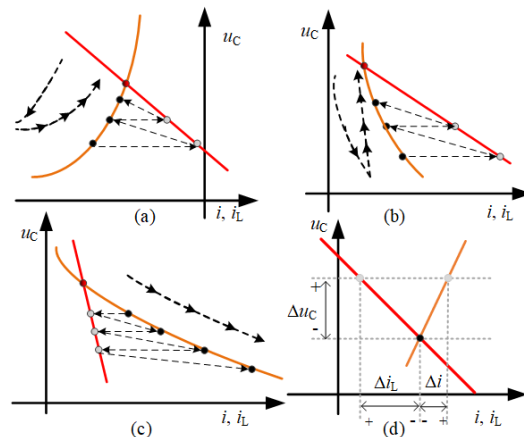
Fig. 5. The schematic diagram of physical interpretation of large signal stability. (a) The first type. (b) The second type. (c) The third type. (d) The physical process of stability.

V. STABILITY DOMAIN OF POWER LOAD LIMIT

As analyzed in Section IV, the reason for system instability under different parameters is that the equivalent constant power load P_e is greater than the maximum load power allowed by the system under a certain circumstance. In this sense, it is necessary to calculate the power load limit that the system can carry under different conditions, which is also meaningful in dc microgrids' energy management.

A. Theoretical Analysis of Power Limit

Considering the circumstance that $P_e > 0$, the maximum

power load P_{lim1} that the system can carry under different parameter groups can be calculated as

$$\begin{cases} P_{\text{lim1}} = \begin{cases} P'_{\max} & r < r_0 \\ P_{\max} & r > r_0 \end{cases} \\ r_0 = \sqrt{L/C} \end{cases} \quad (48)$$

That is, under different parameter groups, the stability criterion is $P_e < P_{\text{lim1}}$. Therefore, once the L, C, and r parameters are fixed, the value of P_e directly determines the stability of the system under stability constraint.

It can be seen from (48), when $r > r_0$, P_{lim1} monotonically decreases as r increases; when $r < r_0$, the trend of P_{lim1} with r cannot be visually seen. Hence, defining

$$\Psi(r) = \frac{4r^2 CL}{\left(L + r^2 C\right)^2} \cdot \frac{U^2}{4r}, \quad (49)$$

the first derivative of (49) is

$$\dot{\Psi}(r) = \frac{CLU^2}{\left(L + r^2 C\right)^2} \cdot \frac{L - 3r^2 C}{L + r^2 C}. \quad (50)$$

It can be seen that P_{lim1} gets the maximum value when $r = r_0 / \sqrt{3}$. Defining the maximum point as $T(r_T, P_T)$, where $r_T = r_0 / \sqrt{3}$, stability margin M_P can be defined as

$$M_P = \left(P_T - P_e\right)/P_T. \quad (51)$$

Furthermore, the nonlinear region $[B_{k,1}, A_{k,1}]$ is constant stable region, but $[A_{k,2}, B_{k,2}]$ is unstable region under ideal conditions. Hence, the system should not operate in the nonlinear region as much as possible. Taking the first quadrant as an example, for a certain r, the bus voltage gradually decreases as P_e increases. Assuming the allowed voltage deviation range is $[\delta_1 U_{\text{rate}}, \delta_2 U_{\text{rate}}]$, then the allowed maximum power load is

$$P_{\text{lim2}} = \delta_i (1 - \delta_i) U_{\text{rate}}^2 / r, i = 1, 2, \quad (52)$$

where, δ_1, δ_2 are the upper and lower deviation limits of the bus voltage separately, and CPLs must satisfy $P_e < |P_{\text{lim2}}|$.

Hence, the power limit P_{lim} constrained by large-signal stability and voltage deviation should be the smaller one between P_{lim1} and $|P_{\text{lim2}}|$, that is

$$P_{\text{lim}} = min\left\{P_{\text{lim1}}, \left|P_{\text{lim2}}\right|\right\}. \quad (53)$$
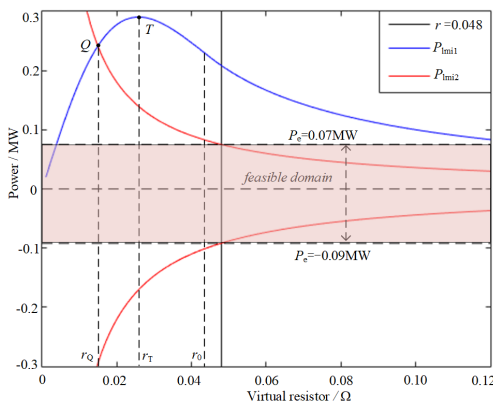

Fig. 6. Feasible domain of CPL with stability and voltage deviation constraints.

B. Case Study

A study case is conducted to illustrate the power limit calculation, where parameters are set in Table II, and constraints are calculated in Table III. Fig. 6 shows the simulation results of C being set as 25 mF. Assuming the intersection point of curve P_{lim2} and curve P_{lim1} is $Q(r_Q, P_Q)$, it can be seen

$$P_{\text{lim}} = \begin{cases} P_{\text{lim2}}, P_e < 0 \\ P_{\text{lim1}}, r < r_Q \ and \ P_e > 0, \\ P_{\text{lim2}}, r \geq r_Q \ and \ P_e > 0 \end{cases} \quad (54)$$

where P_{lim} is shown as the pink area in Fig. 6.

TABLE II
PHYSICAL PARAMETERS FOR SIMULATION

Symbol	Description	Value
U_{rate}	rated voltage	200 V
δ_1, δ_2	lower and upper limits of voltage deviation	0.9, 1.1 p.u.
r	equivalent virtual resistance	0.048Ω
L	equivalent output inductance	0.05mH
C	equivalent capacitance	25mF, 6mF

TABLE III
PARAMETERS CONSTRAINS FOR SIMULATION

Condition	C	P_{lim1}	P_{lim2}	r_Q
$L < r^2 C$	25mF	0.21MW	0.07MW, as $P_e > 0$	0.015Ω
$L > r^2 C$	6mF	0.14MW	-0.09MW, as $P_e < 0$	0.031Ω

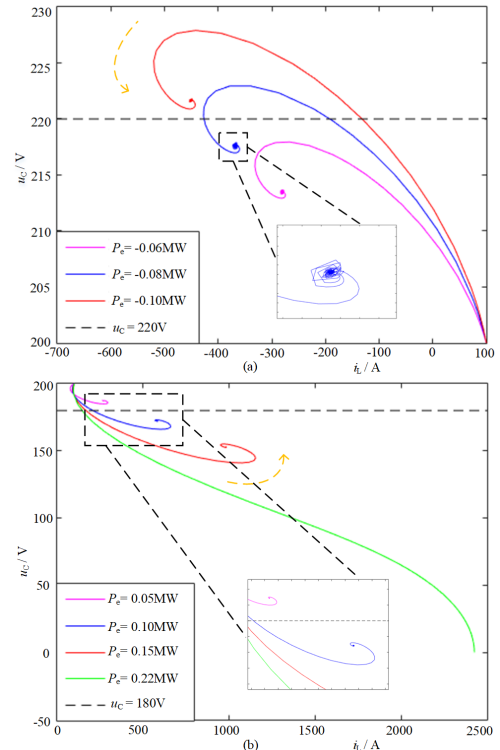Fig. 7. Simulation waveforms under the condition of $L < r^2 C$. (a) Simulation waveforms when $P_e < 0$. (b) Simulation waveforms when $P_e > 0$.

1). Under the condition of $L < r^2 C$. Fig. 7 shows the waveforms of $C = 25\text{mF}$ ($L < r^2 C$). It can be seen from Fig.7(a) that, when $P_e < 0$ the system can converge stably. The waveform of x_{e1} when $P_e > 0$ is shown in Fig. 7(b). Where it can be seen if

$P_e<P_{lim1}$, the system can converge steadily. However, the convergence speed will be gradually slowed down as P_e increases. To be emphasized, when P_e=0.22MW>P_{lim1}, the system cannot converge any more.

From Fig. 7(a) and Fig. 7(b), it also can be concluded that, when $P_e<|P_{lim2}|$, dc voltage can satisfy deviation requirements, otherwise it cannot. Specifically, when P_e= -0.10MW <P_{lim2} in Fig. 7(a), the dc voltage will be larger than 220V; when P_e= 0.10MW>P_{lim2} in Fig. 8(b), the voltage will be lower than 180V. The characteristics shown in Figs.7(a) and (b) are consistent with the theoretical analysis.

2). Under the condition of $L>r^2C$. A case under the condition of $L>r^2C$ is also conducted as shown in Fig. 8, where the capacitance parameter is modified to 6mF, the other parameters remain unchanged.

The waveforms of $P_e<0$ are shown in Fig. 8(a), and the system can converge stably. The waveforms of $P_e>0$ are shown in Fig. 8(b), where the system can converge stably when $P_e<P_{lim1}$. Whereas the system cannot converge when $P_e>P_{lim1}$. Specifically, when P_e= -0.10MW <P_{lim2} in Fig. 8(a), dc voltage will be larger than 220V; when $P_e>P_{lim2}$ (P_e= 0.08MW and P_e= 0.12MW) in Fig. 8(b), dc voltage will be lower than 180V, although the system is stable; when P_e= 0.16MW>P_{lim1}, the system cannot converge stably. These results are consistent with theoretical analysis.
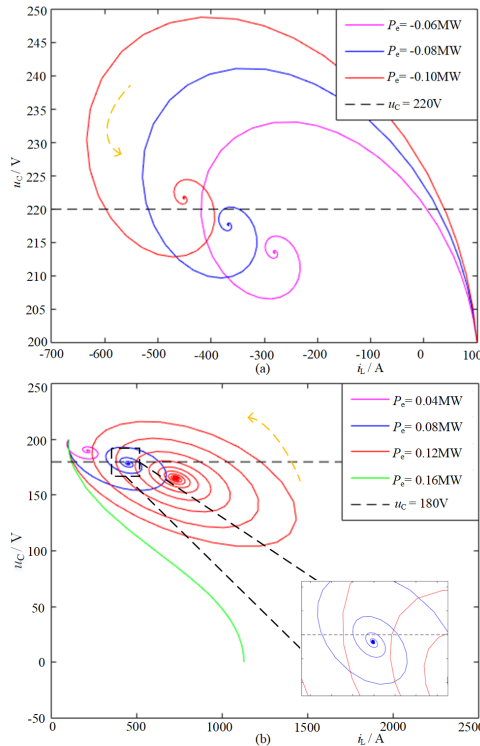

Fig. 8. Simulation waveforms under the condition of $L>r^2C$. (a) Simulation waveforms when $P_e<0$. (b) Simulation waveforms when $P_e>0$.

VI. SIMULATION AND EXPERIMENTAL RESULTS

From the analysis of Section IV, point *a* and *b* are always stable, point *e* is always unstable, and the stability of points *c* and *d* are influenced by system parameters, stability boundary of them are shown in (49). Considering the requirements of

voltage derivation, the power boundary will be changed to be (53). Both boundaries will be verified separately in this part.

An experimental islanded dc microgrid setup, shown in Fig. 9(a) and (b), was used to verify the power load limits under large-signal stability and voltage deviation constraints. The setup consists of a dc source, four parallel-connected DC/DC converters (GCs), *LC* filters, electronic loads (CPLs), and dSPACE controller as well as its monitoring platform. The experimental parameters are shown in Table IV, and the power load limit in the experimental study-cases is analyzed as shown in Fig.9(c) and listed in Table V. Besides, simulations with the same structure and parameters are conducted to make comparisons, as shown in Tables VI and VII. From (41), the power load limits may be influenced by parasitic parameters of the experimental setup. But there is no obvious difference between simulation and experimental results, because the parasitic parameters are small enough compared to *LC* filter.

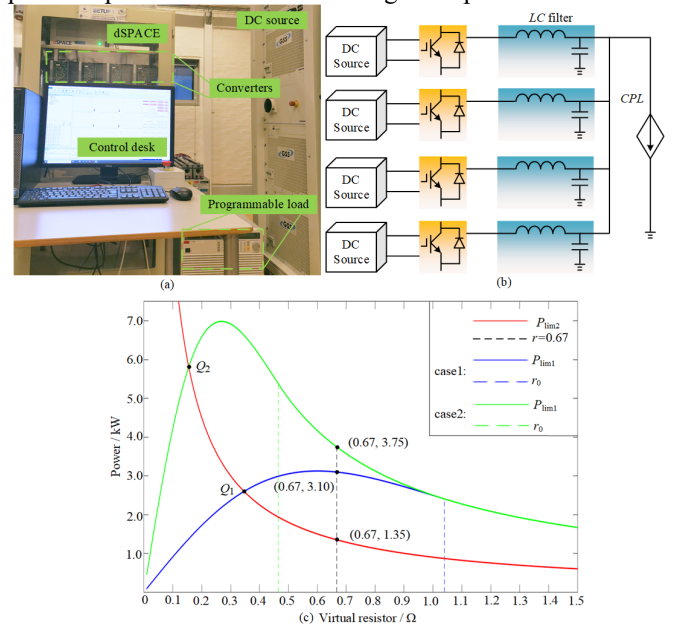

Fig. 9. Experimental platform and cases analysis. (a) Experimental setup in AAU-MG research laboratory. (b)Circuit diagram of testing setup. (c) Power limit analysis of experimental cases.

TABLE IV
PHYSICAL PARAMETERS FOR EXPERIMENT

Converters	Parameters		Equivalent Parameters
GC_1	r_1=2Ω, L_4=2.2mH	case1:C_1=0.1mF case2:C_1=0.6mF	r=0.67Ω
GC_2	r_2=2Ω, L_4=2.3mH	case1:C_2=0.1mF case2:C_2=0.6mF	L=0.54mH
GC_3	r_3=4Ω, L_4=2.2mH	case1:C_3=0.1mF case2:C_3=0.6mF	case1:C=0.5mF
GC_4	r_4=4Ω, L_4=2.0mH	case1:C_4=0.2mF case2:C_4=0.7mF	case2:C=2.5mF

TABLE V
PARAMETERS CONSTRAINS FOR EXPERIMENT

Conditions	P_{lim1}	P_{lim2}	r_Q	Voltage
case1: $L>r^2C$	3.10kW	1.35kW	0.35Ω	U_{rate}=100V δ_1=0.9p.u. δ_2=1.1p.u.
case2: $L<r^2C$	3.75kW	1.35kW	0.16Ω	

TABLE VI
VERIFICATION RESULTS OF CASE 1

Time stages	Load conditions	Voltage states
0.025s~0.05s (T_1~T_2)	1.0kW< P_{lim2}	Stable, and u_C>90V.
0.05s~0.075s (T_2~T_3)	P_{lim2}<1.5kW< P_{lim1}	Stable, but u_C<90V.
0.75s~0.1s (T_3~T_4)	P_{lim2}<2.5kW< P_{lim1}	Stable, but u_C<90V.
0.1s~0.15s (T_4~)	P_{lim1}<3.3kW	Not stable.

TABLE VII
VERIFICATION RESULTS OF CASE 2

Time stages	Load conditions	Voltage states
0.025s~0.05s (T_5~T_6)	1.0kW< P_{lim2}	Stable, and u_C>90V.
0.05s~0.075s (T_6~T_7)	P_{lim2}<1.5kW< P_{lim1}	Stable, but u_C<90V.
0.75s~0.1s (T_7~T_8)	P_{lim2}<2.5kW< P_{lim1}	Stable, but u_C<90V.
0.1s~0.125s (T_8~T_9)	P_{lim2}<3.5kW< P_{lim1}	Stable, but u_C<90V
0.125s~0.16s (T_9~)	P_{lim1}<3.8kW	Not stable.

A. Case1: Verification for $L>r^2C$.

Fig. 10 shows the waveforms of simulation and experimental verifications, where equivalent capacitance value fixed at C=0.5mF, and the parameters P_{lim1}, P_{lim2}, and r_Q calculated as shown in Table V, where $r>r_Q$. The simulation results are shown in Figs. 10(a), (b), and (c), where 1kW, 1.5kW, 2.5kW and 3.3 kW CPLs are connected to the dc microgrid at t=0.025s, t=0.05s, t=0.075s, and t=0.1s respectively. The dc voltage during different time stages is listed in Table VI. It can be seen that, when P_e<P_{lim2}, the bus voltage can satisfy both constraints; when P_{lim2}<P_e<P_{lim1}, the bus voltage can only satisfy stability constraint; when P_{lim1}<P_e, the system is unstable.

In experimental verification, the same loads as those in simulation are connected to the dc microgrid at $t=T_1$, $t=T_2$, $t=T_3$, and $t=T_4$ respectively, and the experimental waveforms are shown in Figs. 10(d), (e), and (f). The detailed information is also listed in Table VI, and the same conclusions as those in simulation results can be concluded. The difference is that at $t=T_4$ because CPLs are larger than the power limit P_{lim1}, the system becomes divergent, resulting in the huge transient current triggering protections, and then the current turns zero, and bus voltage goes back to its nominal value.
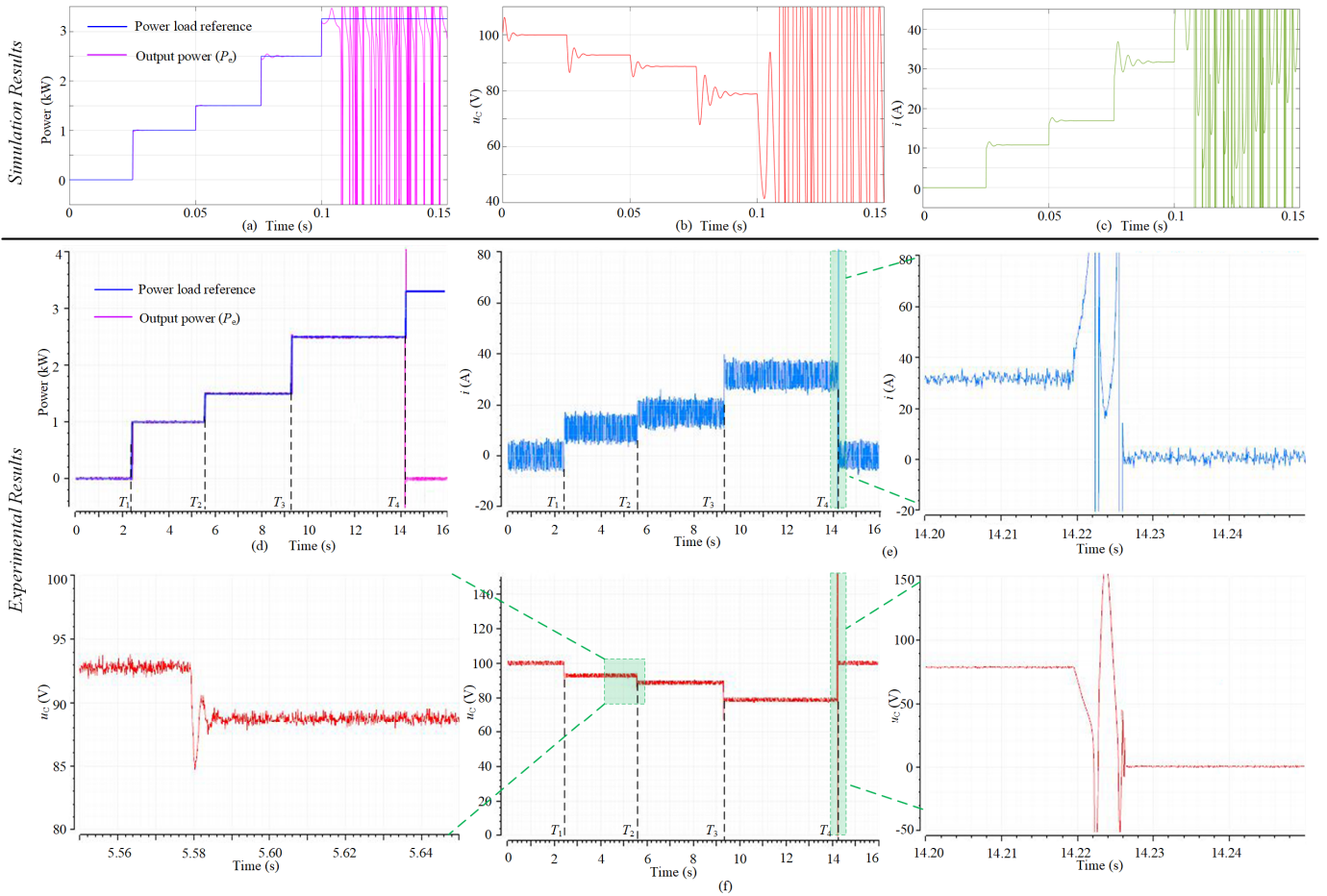

Fig. 10. Simulation and experimental waveforms under the condition of $L>r^2C$. (a)Simulation waveforms of power load and its reference. (b) Simulation waveforms of current of load. (c) Simulation waveforms of dc bus voltage. (d) Experimental waveforms of power load and its reference. (e) Experimental waveforms of current of load. (f) Experimental waveforms of dc bus voltage.

B. Case2: Verification for $L<r^2C$.

In this case, the equivalent capacitance value is fixed at $C=2.5\text{mF}$ to satisfy $L<r^2C$, and constraints are calculated in Table V, where $r>r_Q$. The simulation results are shown in Figs. 11(a), (b), and (c), where 1kW, 1.5kW, 2.5kW, 3.5kW and 3.8 kW CPLs are connected to the dc microgrid at $t=0.025\text{s}$, $t=0.05\text{s}$, $t=0.075\text{s}$, $t=0.1\text{s}$, and $t=0.125\text{s}$ respectively. The dc voltage during different time stages is listed in Table VII. It can be seen that, when $P_e<P_{\text{lim2}}$, the bus voltage can satisfy both constraints; when $P_{\text{lim2}}<P_e<P_{\text{lim1}}$, the bus voltage can only satisfy stability constraint; when $P_{\text{lim1}}<P_e$, the system is unstable.

In experimental verification, the same loads as those in simulation are connected to the dc microgrid at $t=T_5$, $t=T_6$, $t=T_7$, $t=T_8$, and $t=T_9$ respectively, and the experimental waveforms are shown in Figs. 11(d), (e), and (f). The detailed information is also listed in Table VII, and the same conclusions as those in simulation results can be concluded. The difference is that, at $t=T_9$, the system becomes divergent and the huge transient current triggers protections, leading to the consequences of current turning to be zero and bus voltage going back to its nominal value.

Summing up, we can observe that the experimental results are consistent with the theoretical analysis previously done.
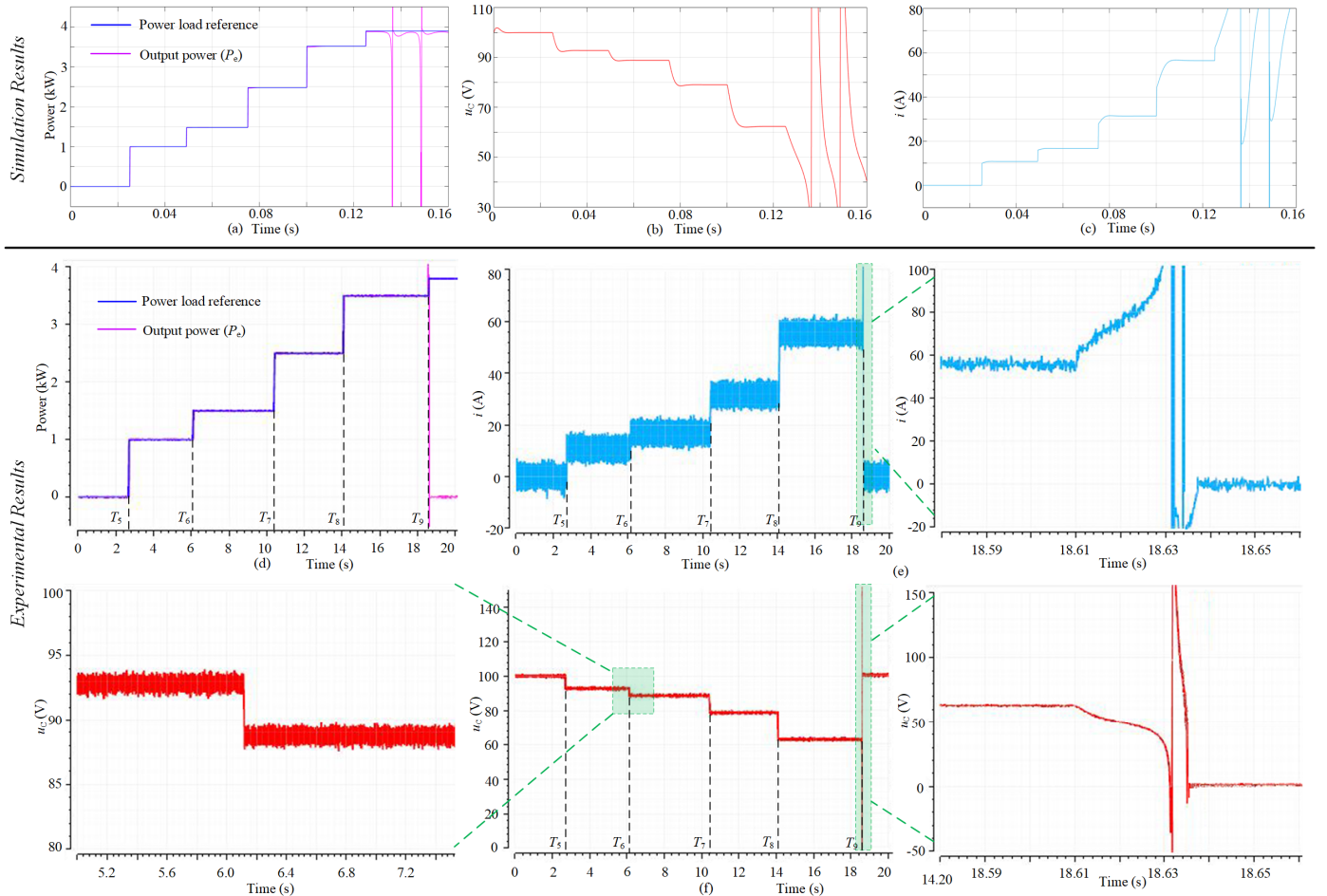

Fig. 11. Simulation and experimental waveforms under the condition of $L<r^2C$. (a)Simulation waveforms of power load and its reference. (b) Simulation waveforms of current of load. (c) Simulation waveforms of dc bus voltage. (d) Experimental waveforms of power load and its reference. (e) Experimental waveforms of current of load. (f) Experimental waveforms of dc bus voltage.

VII. CONCLUSION

This paper presents a large-signal stability analysis from the system-level perspective. Firstly, the normalized equivalent model of a droop-controlled dc microgrid under different operation stages with multiple parallel-connected GCs is proposed. Then, the model is used for the large-signal stability analysis purpose by using the Lyapunov direct method, and the stability criterion is derived mathematically achieving conservatism-free. Besides, MPT method is used to make comparisons with the Lyapunov direct method to enhance the advantages of the latter. Based on the derived criterion, stability

of equilibrium points is discussed and its physical interpretation is firstly explored. Finally, the power load limit is calculated within both constraints of stability and voltage deviations. The load limit calculation is proposing to be expanded in the future of energy management systems. However, there are still some shortages in this paper, that the stability criterion is only suitable for a dc microgrid adopting droop control or voltage constant strategy, and all GCs must be centrally arranged.

APPENDIX

The symbolic expression of $\boldsymbol{H}$ can be expressed as

$$h_a = (L(Cu_C^4 + LP_e^2 + Lu_C^4) - CLP_e u_C^2 r)\,/$$
$$(2(LP_e - Cu_C^2 r)(P_e r - u_C^2)) \tag{1}$$

$$h_b = CLu_C^2(ru_C^2 + P_e)\,/$$
$$(2(LP_e - Cu_C^2 r)(P_e r - u_C^2)) \tag{2}$$

and

$$h_c = Cu_C^2(Cu_C^2 + Lu_C^2 + Cu_C^2 r^2 - LP_e r)\,/$$
$$(2(LP_e - Cu_C^2 r)(P_e r - u_C^2)) \tag{3}$$

The principle of MPT is detailed as follows. For a nonlinear circuit, its mixed potential function can be constructed as

$$P(i,v) = -A(i) + B(v) + (i, \gamma v - \alpha), \tag{4}$$

where i is the inductor current, u is the capacitor voltage, $A(i)$ represents the current potential function, $B(v)$ represents the voltage potential function, γ represents the constant matrix associated with the structure, and α is a constant vector. Besides, it should satisfy

$$\begin{cases} L\dfrac{di}{dt} = \dfrac{\partial P(i,v)}{\partial i} \\ C\dfrac{dv}{dt} = \dfrac{\partial P(i,v)}{\partial v} \end{cases}, \tag{5}$$

which can be used to verify the correctness of energy function.

To illustrate the stability analysis process, several variables need to be defined as

$$\begin{cases} P_i = \dfrac{\partial P(i,v)}{\partial i}, \; P_v = \dfrac{\partial P(i,v)}{\partial v} \\ A_{ii}(i) = \dfrac{\partial^2 A(i)}{\partial i^2}, \; B_{vv}(v) = \dfrac{\partial^2 B(v)}{\partial v^2} \end{cases}. \tag{6}$$

Besides, let μ_1 represent the minimum eigenvalue of matrix $L^{-1/2}A_{ii}(i)\,L^{1/2}$, and μ_2 represent the minimum eigenvalue of matrix $C^{-1/2}B_{vv}(v)\,C^{1/2}$, where L and C are inductance matrix and capacitor matrix, respectively.

If a system is stable it should satisfy the following two conditions. The first one is

$$\mu_1 + \mu_2 > 0. \tag{7}$$

The second one is, when $|i| + |v| \to \infty$,

$$P^*(i,v) = \frac{\mu_1 - \mu_2}{2} P(i,v) + \frac{1}{2} P_i^T (L^{-1} P_i) + \frac{1}{2} P_v^T (C^{-1} P_v) \to \infty. \tag{8}$$

Then, the system is large-signal stable, and all solution circuit will tend to the steady-state value.

In this work, the mixed potential function can be constructed as

$$P(i_L, u_C) = \int_0^{i_L} U_{\text{rate}}\, di_L - \int_0^{i_L} r i_L\, di_L - \int_0^{i_c} u_C\, di_e - \left(i_L - \frac{P_e}{u_C}\right)u_C$$

$$= U_{\text{rate}} i_L - \frac{1}{2} r i_L^2 - \left(u_C i_e - \int_0^{u_c} \frac{P_e}{u_C}\, du_C\right) - i_L u_C + P_e \tag{9}$$

$$= -\frac{1}{2} r i_L^2 + \int_0^{u_c} \frac{P_e}{u_C}\, du_C + i_L(U_{\text{rate}} - u_C)$$

and detailed employment process is illustrated in Section III.

References

[1] Y. Han, K. Zhang, H. Li, E. A. A. Coelho and J. M. Guerrero, "MAS-based distributed coordinated control and optimization in microgrid and microgrid clusters: a comprehensive overview," *IEEE Trans. Power Electron.*, vol. 33, no. 8, pp. 6488-6508, Aug. 2018.

[2] N. Vafamand, M. H. Khooban, T. Dragičević, F. Blaabjerg and J. Boudjadar, "Robust non-fragile fuzzy control of uncertain dc microgrids feeding constant power loads," *IEEE Trans. Power Electron.*, vol. 34, no. 11, pp. 11300-11308, Nov. 2019.

[3] M. Vahedipour-Dahraie, A. Anvari-Moghaddam and J. M. Guerrero, "Evaluation of reliability in risk-constrained scheduling of autonomous microgrids with demand response and renewable resources," *IET Renewable Power Generation*, vol. 12, no. 6, pp. 657-667, Apr. 2018.

[4] J. Lu, M. Savaghebi, Y. Guan, J. C. Vasquez, A. M. Y. M. Ghias and J. M. Guerrero, "A reduced-order enhanced state observer control of dc-dc buck converter," *IEEE Access*, vol. 6, pp. 56184-56191, Sept. 2018.

[5] O. Cornea, G. Andreescu, N. Muntean and D. Hulea, "Bidirectional power flow control in a dc microgrid through a switched-capacitor cell hybrid dc–dc converter," *IEEE Trans. Ind. Electron.*, vol. 64, no. 4, pp. 3012-3022, Apr. 2017.

[6] A. Kwasinski and C. N. Onwuchekwa, "Dynamic behavior and stabilization of DC microgrids with Instantaneous constant-power loads," *IEEE Trans. Power Electron.*, vol. 26, no. 3, pp. 822-834, Mar. 2011.

[7] R. Majumder, "Some aspects of stability in microgrids," *IEEE Trans. Power Syst.*, vol. 28, no. 3, pp. 3243–3252, Aug. 2013.

[8] N. Bottrell, M. Prodanovic, and T. C. Green, "Dynamic stability of a microgrid with an active load," *IEEE Trans. Power Electron.*, vol. 28, no. 11, pp. 5107–5119, Nov. 2013.

[9] F. Zhao, N. Li, Z. Yin and X. Tang, "Small-signal modeling and stability analysis of DC microgrid with multiple type of loads," in *2014 Int. Conf. Power System Technology*, Chengdu, 2014, pp. 3309-3315.

[10] X. Lu, K. Sun, J. M. Guerrero, J. C. Vasquez, L. Huang and J. Wang, "Stability enhancement based on virtual impedance for dc microgrids with constant power loads," *IEEE Trans. Smart Grid*, vol. 6, no. 6, pp. 2770-2783, Nov. 2015.

[11] M. Kabalan, P. Singh and D. Niebur, "Large signal Lyapunov-based stability studies in microgrids: a review," *IEEE Trans. Smart Grid*, vol. 8, no. 5, pp. 2287-2295, Sept. 2017.

[12] A. Guha and G. Narayanan, "Small-signal stability analysis of an open-loop induction motor drive including the effect of inverter deadtime," *IEEE Trans. Ind. Applicat.*, vol. 52, no. 1, pp. 242-253, Jan./Feb. 2016.

[13] F. Katiraei, M. R. Iravani, and P. W. Lehn, "Micro-grid autonomous operation during and subsequent to islanding process," *IEEE Trans. Power Del.*, vol. 20, no. 1, pp. 248–257, Jan. 2005.

[14] Z. Zhang, Q. Chen, R. Xie and K. Sun, "The fault analysis of PV cable fault in dc microgrids," *IEEE Trans. Energy Conversion*, vol. 34, no. 1, pp. 486-496, Mar. 2019.

[15] J. Jiang *et al.*, "A conservatism-free large signal stability analysis method for dc microgrid based on mixed potential theory," *IEEE Trans. Power Electron.*, vol. 34, no. 11, pp. 11342-11351, Nov. 2019.

[16] P. Lin, C. Zhang, P. Wang and J. Xiao, "A decentralized composite controller for unified voltage control with global system large-signal stability in dc microgrids," *IEEE Trans. Smart Grid*, vol. 10, no. 5, pp. 5075-5091, Sept. 2019.

[17] K. Wu, C. W. de Silva and W. G. Dunford, "Stability analysis of isolated bidirectional dual active full-bridge dc–dc converter with triple phase-shift control," *IEEE Trans. Power Electron.*, vol. 27, no. 4, pp. 2007-2017, Apr. 2012.

[18] M. Kabalan, P. Singh and D. Niebur, "A design and optimization tool for inverter-based microgrids using large-signal nonlinear analysis," *IEEE Trans. Smart Grid*, vol. 10, no. 4, pp. 4566-4576, Jul. 2019

[19] M. Mokhtar, M. I. Marei and A. A. El-Sattar, "An adaptive droop control scheme for dc microgrids integrating sliding mode voltage and current controlled boost converters," *IEEE Trans. Smart Grid*, vol. 10, no. 2, pp. 1685-1693, Mar. 2019.

[20] A. P. N. Tahim, D. J. Pagano, E. Lenz and V. Stramosk, "Modeling and stability analysis of islanded dc microgrids under droop control," *IEEE Trans. Power Electron.*, vol. 30, no. 8, pp. 4597-4607, Aug. 2015.

[21] V. Nasirian, A. Davoudi, F. L. Lewis and J. M. Guerrero, "Distributed adaptive droop control for dc distribution systems," *IEEE Trans. Energy Conversion*, vol. 29, no. 4, pp. 944-956, Dec. 2014.

[22] S. Peyghami, H. Mokhtari, P. C. Loh, P. Davari and F. Blaabjerg, "Distributed primary and secondary power sharing in a droop-controlled

LVDC microgrid with merged ac and dc characteristics," *IEEE Trans. Smart Grid*, vol. 9, no. 3, pp. 2284-2294, May 2018.

[23] H. Wang, M. Han, R. Han, J. M. Guerrero and J. C. Vasquez, "A Decentralized current-sharing controller endows fast transient response to parallel DC–DC converters," *IEEE Trans. Power Electron.*, vol. 33, no. 5, pp. 4362-4372, May 2018.

[24] Z. Shuai, C. Shen, X. Liu, Z. Li and Z. J. Shen, "Transient angle stability of virtual synchronous generators using Lyapunov's direct method," *IEEE Trans. Smart Grid*, vol. 10, no. 4, pp. 4648-4661, Jul. 2019.

[25] S. Sanchez and M. Molinas, "Large signal stability analysis at the common coupling point of a DC microgrid: a grid impedance estimation approach based on a recursive method," *IEEE Trans. Energy Conversion*, vol. 30, no. 1, pp. 122-131, Mar. 2015.

[26] X. Lu, K. Sun, J. M. Guerrero, J. C. Vasquez, L. Huang and J. Wang, "Stability enhancement based on virtual impedance for dc microgrids with constant power loads," *IEEE Trans. Smart Grid*, vol. 6, no. 6, pp. 2770-2783, Nov. 2015.

[27] C. Yang, J. Sun, Q. Zhang and X. Ma, "Lyapunov stability and strong passivity analysis for nonlinear descriptor systems," *IEEE Trans. Circuits Syst. I: Regul. Pap.*, vol. 60, no. 4, pp. 1003-1012, Apr. 2013.

[28] H. Kim, S. Kang, G. Seo, P. Jang and B. Cho, "Large-signal stability analysis of dc power system with shunt active damper," *IEEE Trans. Ind. Electron.*, vol. 63, no. 10, pp. 6270-6280, Oct. 2016.

[29] B. P. Loop, S. D. Sudhoff, S. H. Żak and E. L. Zivi, "Estimating regions of asymptotic stability of power electronics systems using genetic algorithms," *IEEE Trans. Control Syst. Technol.*, vol. 18, no. 5, pp. 1011-1022, Sept. 2010.

[30] A. Bacha, H. Jerbi and N. B. Braiek, "An approach of asymptotic stability domain estimation of discrete polynomial systems," in *Proc. Multiconf. Comput. Eng. in Syst. Appl.*, 2006, vol. 1, pp. 288-292.

[31] Brayton, R.K., Moser, J.K. A theory of nonlinear networks. Q. Appl. Math. 1964, 22, 1–33.

[32] K. Sun, L. Zhang, Y. Xing, and J. M. Guerrero, ''A distributed control strategy based on DC bus signaling for modular photovoltaic generation systems with battery energy storage,'' *IEEE Trans. Power Electron.*, vol. 26, no. 10, pp. 3032–3045, Oct. 2011.

[33] D. Wu, F. Tang, T. Dragičević, J. M. Guerrero, and J. C. Vasquez, ''Coordinated control based on bus-signaling and virtual inertia for islanded DC microgrids,'' *IEEE Trans. Smart Grid*, vol. 6, no. 6, pp. 2627–2638, Nov. 2015.

Wenqiang Xie (S'19) was born in Jiangsu, China, in 1993. He received the B.S. degree in North China Electric Power University, Beijing, China, in 2016, where he is pursuing the Ph.D. degree, majoring in electrical engineering.

He is currently a guest Ph.D. student in the Department of Energy Technology, Aalborg University, Aalborg, Denmark. His research interests include power electronics, control, and their applications in dc microgrids.

Minxiao Han (M'05–SM'18) was born in Shannxi, China, in 1963. He received his Ph.D. from North China Electric Power University (NCEPU). He was a visiting Ph.D. student with Queen's University of Belfast, U.K. and a post-doctoral fellow with Kobe University, Japan. He is presently the Director of Institute of Flexible Electric Power Technology of NCEPU. He has been the leader in projects consigned by National Nature Science Foundation of China, National Educational Ministry, and enterprises. He has four published books and more than 100 refereed publications in journals and conferences. His research interests are the applications of power electronics in power system including HVDC, FACTS, power conversion and control.

Wenyuan Cao (S'19) was born in Hunan, China, in 1994. He received the B. S. degree in North China Electric Power University, Beijing, China, in 2017, where he is pursuing the Ph.D. degree. His research interests include hybrid AC/DC distribution network and its control.

Josep M. Guerrero (S'01–M'04–SM'08–F'15) received the B.S. degree in telecommunications engineering, the M.S. degree in electronics engineering, and the Ph.D. degree in power electronics from the Technical University of Catalonia, Barcelona, in 1997, 2000 and 2003, respectively. Since 2011, he has been a Full Professor with the Department of Energy Technology, Aalborg University, Denmark, where he is responsible for the Microgrid Research Program. From 2014, he is Chair Professor in Shandong University. Since 2015, he has been a Distinguished Guest Professor at Hunan University. Since 2016, he has been a visiting professor fellow at Aston University, UK, and a guest Professor at the Nanjing University of Posts and Telecommunications. From 2019, he became a Villum Investigator by The Villum Fonden, which supports the Center for Research on Microgrids (CROM) at Aalborg University, where he is the Founder and Director. He has published more than 500 journal papers in the fields of microgrids and renewable energy systems, which are cited more than 50,000 times. His research interests include different microgrid aspects, including power electronics, distributed energy-storage systems, hierarchical and cooperative control, energy management systems, smart metering and the internet of things for ac/dc microgrid clusters and islanded minigrids, with a special focus on microgrid technologies applied to offshore wind and maritime microgrids for electrical ships, vessels, ferries, and seaports. Prof. Guerrero is an Associate Editor for a number of IEEE Transactions. He received the Best Paper Award of the IEEE TRANSACTIONS ON ENERGY CONVERSION for the period 2014–2015, the Best Paper Prize of IEEE-PES in 2015, the Best Paper Award of the IEEE JOURNAL OF POWER ELECTRONICS in 2016. From 2014 to 2019, he was awarded by Clarivate Analytics (former Thomson Reuters) as Highly Cited Researcher. In 2015, he was promoted as a Fellow at the IEEE for his contributions on distributed power systems and microgrids.

Juan C. Vasquez (M'12-SM'14) received the B.S. degree in electronics engineering from the Autonomous University of Manizales, Manizales, Colombia, and the Ph.D. degree in automatic control, robotics, and computer vision from Barcelona Tech-UPC, Spain, in 2004 and 2009, respectively. In 2011, He was Assistant Professor and in 2014, Associate Professor at the Department of Energy Technology, Aalborg University, Denmark. In 2019, He became Professor in Energy Internet and Microgrids and currently He is the Co-Director of the Villum Center for Research on Microgrids (see crom.et.aau.dk). He was a Visiting Scholar at the Center of Power Electronics Systems (CPES) at Virginia Tech, USA and a visiting professor at Ritsumeikan University, Japan. His current research interests include operation, advanced hierarchical and cooperative control, optimization and energy management applied to distributed generation in AC/DC Microgrids, maritime microgrids, advanced metering infrastructures and the integration of Internet of Things and Energy Internet into the Smart Grid. Prof. Vasquez is an Associate Editor of IET POWER ELECTRONICS and a Guest Editor of the IEEE TRANSACTIONS ON INDUSTRIAL INFORMATICS Special Issue on Energy Internet. Prof. Vasquez was awarded as Highly Cited Researcher by Thomson Reuters from 2017 to 2019 and He was the recipient of the Young Investigator Award 2019. He has published more than 450 journal papers in the field of Microgrids, which in total are cited more than 19000 times. Dr. Vasquez is currently a member of the IEC System Evaluation Group SEG4 on LVDC Distribution and Safety for use in Developed and Developing Economies, the Renewable Energy Systems Technical Committee TC-RES in IEEE Industrial Electronics, PELS, IAS, and PES Societies